Evaluating the Utility of Sentinel-1 in a Data Assimilation System for Estimating Snow Depth in a Mountainous Basin

Bareera N. Mirza[1], Eric E. Small[2], Mark S. Raleigh[1]

[1]College of Earth, Ocean, and Atmospheric Sciences, Oregon State University, Corvallis, OR, USA

[2]Geological Sciences, University of Colorado, Boulder, CO, USA

Correspondence to: Bareera N. Mirza (mirzaba@oregonstate.edu)

Abstract:

Seasonal snow plays a critical role in hydrological and energy systems, yet its high spatial and temporal variability makes accurate characterization challenging. Historically, satellite remote sensing has had limited success in mapping snow depth and snow water equivalent (SWE), particularly in global mountain areas. This study evaluates the temporal and spatial accuracy of recently developed snow depth retrievals from the Sentinel-1 (S1) C-band spaceborne radar and their utility within a data assimilation (DA) system for characterizing mountain snowpack. The DA framework integrates the physics-based Flexible Snow Model (FSM2) with a Particle Batch Smoother (PBS) to produce daily snow depth maps at a 500-meter resolution using S1 snow depth data. The S1 data were evaluated from 2017 to 2021 in and near the East River Basin, Colorado, using daily data at 12 ground-based stations for temporal evaluation and four LiDAR snow depth surveys from the Airborne Snow Observatory (ASO) for spatial evaluation. The analysis revealed significant inconsistencies in temporal and spatial errors of S1 snow depth, with higher spatial errors. Errors increased with time, especially during ablation periods, with an average temporal RMSE of 0.40 m. In contrast, the spatial RMSE exceeded 0.7 m, and S1 had poor spatial agreement with ASO LiDAR ($R^2 < 0.3$). Experiments with DA window sizes showed minimal performance differences for full-season and early-season windows. Joint assimilation of S1 snow depth with MODIS Snow Disappearance Date (SDD) yielded similar temporal errors but degraded performance in space relative to assimilating S1 alone, while SDD assimilation alone performed best spatially. While S1 may perform better in other regions or snow conditions, our findings are consistent with findings from other error analyses across the Western U.S. and suggest S1 has limited potential to improve snow DA in the East River Basin, specifically. Future work should address retrieval biases, refine algorithms, and consider other snow datasets in the DA system to improve snow depth and SWE mapping in diverse snow environments globally.

1. Introduction

Seasonal snow is a natural freshwater reservoir for around 20% of the world's population (Barnett et al., 2005) and plays a key role in the global energy budget. Global mapping of snow characteristics like snow water equivalent (SWE) is a critical challenge, especially in steep and complex mountain terrain where SWE has high spatial and temporal variability (Clark et al., 2011; Kinar and Pomeroy, 2015; López-Moreno et al., 2011; Raleigh and Small, 2017). The snow community has been developing ground measurement, modeling, and remote sensing techniques through campaigns (e.g., NASA SnowEx) to advance our capabilities for estimating snow characteristics. Despite these efforts, there is still no globally available snow dataset in mountainous terrain at appropriate resolutions (~100s m or finer). Where point SWE measurements exist (e.g., stations), the high spatiotemporal variability makes it challenging to extrapolate SWE across global mountain environments (Cluzet et al., 2022; Dozier, 2011; Dozier et al., 2016; Elder et al., 1998; Grünewald et al., 2010; Herbert et al., 2024; Molotch and Bales, 2006). Improving our ability to estimate SWE in complex mountain regions requires continued advancements in global snow measurement and modeling techniques.

Optical satellite remote sensing has been used extensively in estimating snow properties. Spaceborne photogrammetry is effective for retrieving high-resolution snow depth (Deschamps-Berger et al., 2022; Marti et al., 2016; McGrath et al., 2019). However, this estimation is unavailable during cloudy periods and in dense forests. Spaceborne laser altimetry, such as ICESat and ICESat-2 has demonstrated some capability in mapping snow depth (Besso et al., 2024; Deschamps-Berger et al., 2023; Hu et al., 2022; Treichler and Kääb, 2017), but errors are high and spatial-temporal sampling is sparse. Optical remote sensing techniques for snow cover area (SCA) mapping, using sensors like Landsat, MODIS, and Sentinel-2, permit monitoring snow cover extent (e.g., Stillinger et al., 2023). However, accurate mapping is hindered by cloud cover or dense vegetation (Aalstad et al., 2020). While optical remote sensing cannot measure SWE or snow depth, the information on SCA depletion can guide model-based estimates of SWE (e.g., Margulis et al., 2019; Rittger et al., 2016).

Passive microwave remote sensing retrievals have traditionally been used to retrieve snow depth (Foster et al., 1996; Kelly et al., 2003) and SWE (Chang et al., 1987; Derksen et al., 2005) however,

75 its coarse spatial resolution (up to ~25km) cannot capture the variability of mountain snowpack,
76 and its accuracy is reduced in wet or deep snow conditions (over 1m; Luojus et al., 2021). In
77 contrast, active microwave remote sensing, such as Sentinel-1's (S1) C-band synthetic aperture
78 radar (SAR) backscatter data, has shown potential in mapping mountain snow depth at a scale of
79 0.5 km or finer (Lievens et al., 2019, 2022). S1 data have the potential to improve understanding
80 of mountain snow distributions and associated processes like orographic precipitation dynamics
81 and streamflow generation (Brangers et al., 2024; Girotto et al., 2024). Nevertheless, S1 snow
82 depth data has two fundamental challenges: (1) the data are not temporally continuous (i.e., gaps
83 due to satellite repeat or removed pixels flagged as wet snow), and (2) snow density is required to
84 convert snow depth to SWE (snow depth to SWE = density x snow depth). Two possible solutions
85 are: (1) machine learning (Broxton et al., 2024, 2019; Dunmire et al., 2024) or (2) data assimilation
86 (DA) frameworks (Smyth et al., 2022; Alonso-González et al., 2022). Machine learning has been
87 used to produce temporally continuous snow depth data utilizing the S1 snow depth data (Broxton
88 et al., 2024), but may require region-specific training due to geographic variations in snowpack
89 characteristics, making it less suitable for global mapping. In contrast, the assimilation of remotely
90 sensed snow depth can improve snowpack estimation (including estimates of snow density) and
91 provide temporally continuous data (Deschamps-Berger et al., 2022; Girotto et al., 2020; Largeron
92 et al., 2020; Margulis et al., 2015; Smyth et al., 2019, 2020) . However, prior S1 DA studies have
93 typically been limited to early-season assimilation, (Brangers et al., 2024; De Lannoy et al., 2024;
94 Girotto et al., 2024) and little to no work has yet explored the full-season potential of the DA
95 pathway for SWE mapping using S1 snow depth.

96 While S1 snow depth data have the potential to guide DA systems to produce comprehensive
97 spatiotemporal mountain SWE maps, there have been discrepancies in the reported spatial and
98 temporal errors, which prompt questions about its reliability. Independent evaluations have
99 reported large errors (Broxton et al., 2024; Dunmire et al., 2024; Hoppinen et al., 2024; Sourp et
100 al., 2025) relative to LiDAR snow depth from Airborne Snow Observatory (ASO; Painter et al.,
101 2016) surveys and gridded snow datasets (Broxton et al., 2024). Sourp et al. (2025) found that S1
102 retrievals exhibit no clear error pattern but consistently underestimate snow depth, particularly
103 before and after the melt period. Broxton et al. (2024) found mean bias from 0.27m to 0.25m when
104 compared against ASO LiDAR flights, depending on the removal of "flagged wet pixels".
105 Hoppinen et al. (2024) found that these flagged pixels do not fully eliminate wet pixels and remove

106 some shallow dry snow pixels, resulting in a loss of usable data. Hoppinen et al. (2024) showed
107 little to no spatial correlation between S1 and LiDAR data, contrary to R ~0.52 reported by Lievens
108 et al. (2019) over the Northern Hemisphere. Evaluation studies (Broxton et al., 2024; Hoppinen et
109 al., 2024) validate S1 data on a handful of dates near/after peak SWE with LiDAR surveys in the
110 western U.S., while Lievens et al. (2022) conducted validation against point-scale time series at
111 1000s of locations in the European Alps and other global mountain ranges. Previous studies have
112 shown that C-band S1 is ineffective near or after peak SWE due to the high liquid water content in
113 the snowpack, which leads to the attenuation and absorption of microwave energy (Gagliano et al.,
114 2023; Nagler et al., 2016), leading to increased uncertainties in the retrieved snow depth. Thus, the
115 spatial evaluation data (airborne LiDAR) are mostly available later in the snow season when S1
116 data are less reliable. Gascoin et al. (2024) highlights this limitation and recommends two strategies
117 using S1 snow depth in a DA system: (1) assimilating S1 only during the early season when snow
118 is dry, and (2) implementing a joint assimilation of S1 snow depth along with other remote sensing
119 data (e.g., the snow disappearance date from optical snow-covered area data). To our knowledge,
120 no studies have tested these strategies with S1 snow depth.

121 This paper aims to understand the spatiotemporal error discrepancies in S1 snow depth and assess
122 how these data can be used in a DA system, both alone and in combination with other remote
123 sensing data. First, we evaluate the S1 snow depth data (500 m resolution) using ground-based data
124 at 12 sites and four airborne LiDAR flights in the well-studied East River Basin (Colorado, USA).
125 Second, we develop a DA system using a physics-based model leveraging the recent development
126 of the open-source toolbox Multiple Snow Data Assimilation System (MuSA) (Alonso-González
127 et al., 2022) and deploy our DA system in a cloud-based environment. Using this system, we test
128 whether assimilation of S1 snow depth across the full season (all observations) versus early season
129 (when it is assumed to be most reliable) improves snow depth estimation in time and space, relative
130 to snow simulations without assimilation. Finally, we test the joint assimilation of S1 snow depth
131 and Moderate Resolution Imaging Spectroradiometer (MODIS) snow disappearance date (SDD)
132 (Crumley et al., 2020) following the recommendation of Gascoin et al. (2024). We address three
133 research questions:

1. How do Sentinel-1 snow depth errors vary across space and time?

2. What is the relative value of using full-season Sentinel-1 data compared to early-season data in a data assimilation framework?

3. Can the joint assimilation of Sentinel-1 snow depth and MODIS snow disappearance date enhance DA accuracy?

2. Study Location and Data:

2.1. Study Location:

The study area is the East River Basin, Colorado (ERB Figure 1a), which has a ~748 km² area and features alpine tundra at higher elevations, montane forest at middle elevations, and prairie snow climates in lower elevation valleys (Sturm and Liston, 2021). The ERB has an average elevation of 3266m with 1,420 m topographic relief. It is characterized by cold winters, with a mean annual temperature of 0°C and mean annual precipitation of 1200 mm, mostly as snow (Daly et al., 1994; Hubbard et al., 2018). This cold, dry climate, along with moderate canopy cover, makes the ERB a representative testbed for assessing S1, which tends to struggle in complex terrain (e.g., wet snow, dense forest; Lievens et al., 2019). Furthermore, it has been well-studied and has extensive validation data through multiple scientific field campaigns, such as NASA SnowEx, ASO, the DOE SAIL (Feldman et al., 2023), and NOAA SPLASH (De Boer et al., 2023). It also includes long-term NRCS SNOTEL sites within the basin (Butte) and nearby (e.g., Schofield Pass). In addition, ground measurements are available through a research site established in late 2018 on Snodgrass Mountain (Bonner et al., 2022), which was included in the 2020 NASA SnowEx campaign. Additionally, the ERB has been mapped by airborne LiDAR flight surveys carried out by ASO (Painter et al., 2016), which provided 50 m snow depth measurements twice in two study years (2018 and 2019). The study period spans water years 2018-2021, coinciding with the availability of S1 data and ASO data.
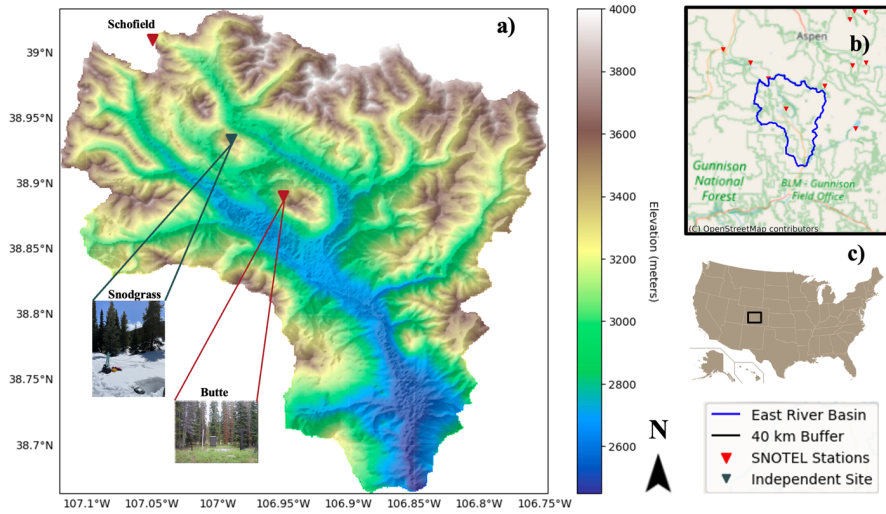
Figure 1: (a) Elevation map of the East River Basin (Jarvis et al., 2008) with Snodgrass and SNOTEL (USDA,NRCS, 2024) stations within and near the basin. **(b)** SNOTEL stations within 40km from the boundary of the basin. **(c)** Location of the East River Basin shown relative to the Western United States.

2.2. Data

2.2.1. Meteorological forcing:

ECMWF ERA5-Land reanalysis data (Copernicus Climate Change Service, 2019; Hersbach et al., 2020) are used as the source of meteorological forcing data as they are available globally at a 0.1-degree (9 km) resolution hourly from 1950 to the present. The data, accessed from Google Cloud Storage, include incoming shortwave and longwave radiation [W m^{-2}], total precipitation (liquid and solid) [kg m^{-2} s^{-1}], surface atmospheric pressure [Pa], 2 m air temperature [K], 2 m relative humidity [%], and 10 m wind speed [m s^{-1}]. The data were not downscaled to the S1 500 m resolution because the DA approach implicitly accounts for fine-scale variability during assimilation (see below). In this implementation, a model ensemble is first generated at the original 9 km resolution and then regridded by nearest neighbor to 0.5 km resolution before applying the Particle Batch Smoother (PBS), effectively capturing the downscaling process (Bachand et al., 2025; Girotto et al., 2024; Smyth et al., 2019, 2020).

2.2.2. Sentinel-1 Snow Depth:

177 We analyzed the 500 m S1 snow depth product (Lievens et al., 2022), which is available across
178 mountainous regions of the Northern Hemisphere from 2016 to 2021. This dataset is derived from
179 C-Band (5.4 GHz) SAR backscatter measurements collected by the ESA Sentinel-1A and Sentinel-
180 1B satellites. The snow depth retrieval algorithm utilizes temporal variations in the ratio between
181 cross-polarized and co-polarized backscatter signals, which are sensitive to snow depth in dry
182 snow. Snow depth retrievals have reported mean absolute errors of 0.18m over the Northern
183 Hemisphere (Lievens et al., 2019). However, the S1 performance degrades in challenging
184 conditions (snow that is wet, shallow, patchy, or in forests) with a mean absolute error of about
185 1.3m at a depth of 3.5m and above (Lievens et al., 2022). Evaluation and development of this
186 dataset is ongoing. The latest 500m dataset includes a quality flag for wet snow conditions, which
187 has potential use for identifying and removing pixels with higher retrieval errors, particularly
188 during the ablation season. Wet snow leads to the absorption and attenuation of radar signals, which
189 makes snow depth mapping unreliable. The frequency of observations varies by region depending
190 on the satellite overpass schedule. However, the dataset offers temporal resolution primarily on a
191 daily to weekly basis, with most intervals being less than one week over the ERB.

192 ### 2.2.3. Snow Disappearance Date (SDD):
193 We conduct multiple DA experiments (see Section 3.4), some of which utilize SDD as an input in
194 the assimilation to test whether S1 provides new information. We utilize SDD rather than daily
195 time series of snow-covered area for simplicity, and recognizing that SDD has been found to have
196 high correlation with maximum SWE (Trujillo and Molotch, 2014). We also include SDD in a
197 joint assimilation experiment to inform our model about end-of-season snowpack conditions (i.e.,
198 Gascoin et al., 2024), especially since S1 is only available through April 30th and has limitations
199 during the melt season due to signal attenuation (Lievens et al., 2022). We derive SDD from
200 different sources depending on the experiment. For the temporal evaluations, we derived SDD
201 from SNOTEL by finding the first zero snow depth value after peak snow depth. For spatial
202 evaluations, we derived SDD from MODIS snow cover data using annual summary metrics based
203 on the daily Normalized Difference Snow Index (NDSI) from the MOD10A1 product with a
204 threshold of 0.15, leveraging the SnowCloudMetrics algorithm implemented on Google Earth
205 Engine (Crumley et al., 2020). The MODIS SDD is determined by identifying the last five snow-
206 free days (backward approach) preceded by at least five consecutive snow-covered days. This

207 approach minimizes the impact of transient late-season snow events while ensuring a consistent
208 detection of snow disappearance.

209 ## 2.2.4. Evaluation Data:

210 We conduct temporal and spatial evaluations of snow depth, both prior to S1 assimilation and
211 posterior to assimilation. Temporal evaluation utilizes daily snow depth from 11 NRCS SNOTEL
212 stations within 40 km of the basin. Since the S1 change detection algorithm was optimized using
213 SNOTEL data (Lievens et al., 2019), an independent research site at Snodgrass Mountain (Figure
214 1) was also utilized to assess the reliability of S1 snow depth time series away from SNOTEL sites.
215 The Snodgrass Mountain site provides snow depth data, along with numerous monthly in situ snow
216 pit measurements from February to May. These snow pits, located in both open and forested areas
217 with a spatial extent of 1 km, are ideal for evaluating the 500 m S1 grid. S1 and posterior snow
218 depths are evaluated against observations from these sites for WYs 2018–2021 for SNOTEL sites
219 and 2019–2021 at the Snodgrass site.

220 The spatial evaluation uses four ASO LiDAR flights, with 50 m snow depth data collected near
221 peak SWE (i.e., late March / early April) and in the mid-melt season (i.e., May or June) in 2018
222 and 2019 over the ERB. The data were resampled to match the 500 m S1 grid resolution using
223 bilinear interpolation.

224 # 3. Methods:

225 ## 3.1. DA Methodology

226 DA integrates model estimates with observations to estimate the most representative state of a
227 system (e.g., SWE) with uncertainty. DA can account for observational uncertainty (e.g., S1 snow
228 depth, MODIS SDD), and some DA approaches can provide physically consistent estimates of
229 multiple snow states when implemented with a physically-based snow model. In this study, we
230 develop and deploy a Python-based DA system in the Google Cloud Platform. Within the cloud,
231 the system accesses ERA-5 Land meteorological data and uses it as input forcing into the MuSA
232 toolbox, which communicates with the physically-based Flexible Snow Model version 2 (FSM2)
233 model to generate ensembles of model simulations at a 9-km spatial resolution. The snow model
234 ensembles from MuSA are combined with snow observations (e.g., S1 snow depth and/or SDD)

235 via the particle batch smoother (PBS). Through assimilation of snow data with a wide ensemble
236 (section 3.2), PBS also serves as a downscaling technique(Bachand et al., 2025) from the 9-km
237 ERA5-Land forcings to the 500 m grid. The flow chart in Figure 2 and the sections below detail
238 the key components.

239
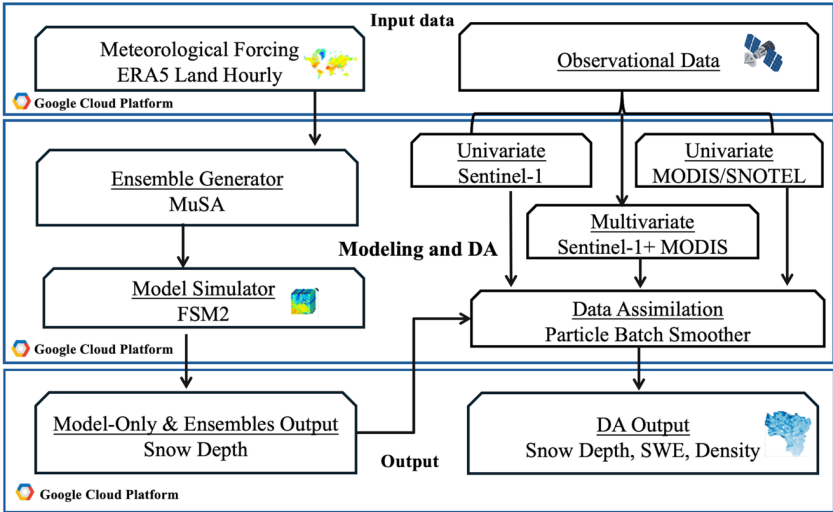
240 **Figure 2**. Flowchart illustrating the input, model, and DA framework, and outputs (top to bottom).

3.2. Snow Model and Ensemble Generation

242 FSM2 (Essery, 2015; Essery et al., 2024) is a multi-physics model that simulates the mass and
243 energy balances of snow on the ground (including under forest canopies), employing three snow
244 layers by default. The model incorporates conservation equations for liquid water, ice, and internal
245 energy, offering a detailed representation of snowpack processes. FSM2's flexibility permits
246 independent activation or deactivation of parameterizations, facilitating a range of model
247 configurations (Essery, 2015; Essery et al., 2024). We utilize the most complex configuration of
248 FSM2 to simulate internal snowpack processes, which we now briefly summarize. Albedo is
249 calculated based on snow age, decreasing its value with time, and increasing it with fresh
250 snowfalls. Snowpack thermal conductivity is determined by snow density, which is computed
251 based on overburden and thermal metamorphism. Turbulent energy fluxes are computed based on
252 bulk aerodynamic theory, and Monin-Obukhov adjustment for atmospheric stability is activated as

253 part of the calculation process. Meltwater percolation in the snowpack is computed using
254 gravitational drainage. The selected configuration has demonstrated success in related DA studies
255 (Smyth et al., 2022).

256 MuSA is an open-source, ensemble-based snow DA tool designed to assimilate multiple
257 observations with FSM2 while considering various sources of forcing and measurement
258 uncertainty (Alonso-González et al., 2022). We use MuSA to generate ensembles of FSM2 at a
259 point scale. We perturbed the 9-km ERA5-Land hourly meteorological forcing data by drawing
260 spatially independent, random perturbation parameters from a logitnormal distribution for
261 precipitation (to avoid negative values) and from a normal distribution for temperature and LW
262 radiation (Table 1). For precipitation, we applied bounds of [0, 4] with $\mu = 0$ and $\sigma = 1$, capturing
263 a wide range of basin-scale variability. For temperature and LW, we applied $\mu = 0$ and $\sigma = 2.5$ and
264 $\mu = 0$ and $\sigma = 20.8$, respectively. Several combinations of bounds, standard deviation, and mean
265 values were tested, and the final configuration was selected to be broader than typical ranges to
266 account for the fact that ERA5-Land was not downscaled prior to assimilation and to better
267 represent spatial variability in the East River Basin, Colorado. We tested and visualized the
268 resulting spread to confirm realistic precipitation, temperature, and LW scenarios, and found that
269 more than 98% of observed S1 snow depth values fell within the ensemble bounds during
270 assimilation. Overall, this perturbation strategy was chosen to ensure the ensemble spans a wide
271 range of meteorological conditions and captures a realistic range of possible snow depths.

272 **Table 1.** Generation of perturbed inputs for each particle member.

Variable	Unit	Adjustment	Distribution	Lower Bound	Upper Bound	Std. dev.	Mean
Precipitation	mm/h	Multiplicative	Logit-normal	0	4	1	0
Longwave radiation	W/m^2	Additive	Normal	-	-	20.8	0
Temperature	°C	Additive	Normal	-	-	2.5	0

273 Once the forcing data are perturbed, MuSA runs FSM2 to generate an ensemble of distinct snow
274 simulations. Similar to Bachand et al. (2025), we used 100 ensemble members (particles) to ensure
275 computational efficiency while adequately capturing the variability in the prior distribution. For

276 each particle, we record the SDD (i.e., the first snow-free date after peak snow depth), for use in
277 multiple DA experiments (see Section 3.4).

3.3. Particle Batch Smoother – DA Algorithm

279 Once the ensembles are generated, we assimilate snow observations (e.g., snow depth and/or SDD)
280 using the PBS algorithm. Separately, we tested other DA approaches, namely the Particle filter
281 (PF), both with constant and dynamic errors, the latter of which increases errors in time as revealed
282 in our temporal analysis as SNOTEL sites (Figure 4). Despite having constant observational error,
283 PBS had lower RMSE than both PF implementations (Supplement Figure S1, Table S1),
284 particularly during the ablation seasons, likely due to its smoothing properties. We therefore
285 selected the PBS with temporally constant snow depth error for subsequent analysis. PBS is well-
286 suited as a downscaling tool as well (Bachand et al., 2025), further motivating its selection in this
287 study.

288 PBS employs a Bayesian approach, representing state variables like snow depth and SDD through
289 a collection of particles, where each particle represents a possible system state. For observations
290 within the assimilation window (e.g., snow season), PBS updates particle weights based on their
291 likelihood of representing the true state, using the likelihood function from Margulis et al. (2015).
292 This process combines the prior probability density function (PDF) with the likelihood to estimate
293 the posterior PDF of snowpack variables, such as snow depth and SWE:

294
$$p_{Z|Y}\left(Z_j Y\right)=p_v\left(Z-M_j^-\right)=\frac{1}{\sqrt{(2\pi)^{N_{obs}}|C_v|}}\times \exp\left[-0.5\left(Z-M_j^-\right)^{\top}C_v^{-1}\left(Z-M_j^-\right)\right]$$
    Equation (1)

295 Where $p_{(Z|Y(Z|Y))}$ is the likelihood function, which represents the probability of observing the
296 measurement $p_V(V)$ is the probability density function (PDF) of the measurement error vector V,
297 Z is the observed measurement (e.g., S1 snow depth, MODIS SDD), M_j is the modeled snow
298 variable (e.g., snow depth or SDD), and C_v is the error covariance matrix of the measurement error
299 vector V, which represents the uncertainty in the measurement.

3.4. DA Experiments

302 To address Research Questions 2 and 3, we conducted four experiments, building on the findings
303 of Research Question 1 (S1 error analysis). The DA experiments are as follows (Figure 3):

304   1. Snow Depth (**Hs**) **F**ull Window **(Hs-F):** Assimilation of all Hs, including dry and wet snow
305   pixels, from November 15th to April 30th. S1 has data only until April 30th, and 83% of
306   S1 data points before November 15th have zero or less than 10cm snow depth values. Thus,
307   we call Hs-F a full-window experiment.

308   2. Snow Depth (**Hs**) **E**arly Window **(Hs-E):** Assimilation of early-season (November 15th to
309   January 15th) Hs, where the early window has a lower observational error than the full
310   window (based on error analysis, section 4.1).

311   3. Joint Assimilation of SDD and Snow Depth in the **F**ull Window **(SDD+Hs-F):** Combined
312   assimilation of SDD and Hs over the same window as Hs-F. SDD data were derived from
313   SNOTEL for temporal evaluation and MODIS for spatial evaluation.

314   4. **S**now **D**isappearance **D**ate Only **(SDD):** Assimilation of SDD data alone, derived from
315   SNOTEL (temporal evaluations) or MODIS (spatial evaluations). This serves as a baseline
316   or control experiment to understand whether S1 snow depth adds new information.

317 SDD is the baseline experiment, and each of the experiments are evaluated against 12 ground-
318 based stations temporally and 4 ASO LiDAR flights spatially (Section 2.2.2). In experiments Hs-
319 F, Hs-E, and SDD+Hs-F, the observational uncertainty value (Equation 1) for S1 snow depth is the
320 RMSE when evaluated against SNOTEL for all four years. The SDD observational uncertainty is
321 set to five days, consistent with the retrieval algorithm in SnowCloudMetrics (Crumley et al., 2020;
322 Slater et al., 2013). In the joint assimilation (SDD+Hs-F), both datasets are weighted equally to
323 balance their respective influence in DA. The joint likelihood is computed in log space under the
324 assumption of independence between the S1 snow depth and SDD observations. This equal-weight
325 approach for joint assimilation is necessary for two reasons: (1) there is an imbalance in the number
326 of observations for Hs (dozens of observations) versus SDD (1 value) for each location and year,
327 and (2) the Hs time series exhibits temporal autocorrelation.
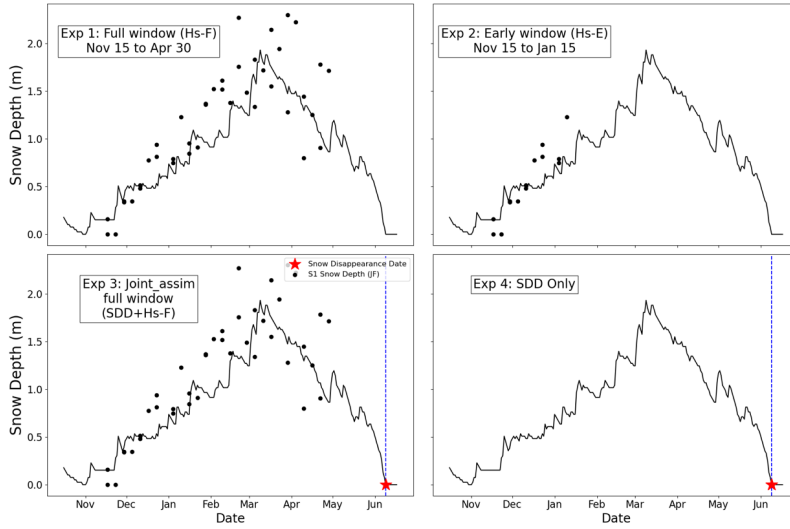
Figure 3. Conceptual illustration of four experiments. Black dots indicate S1 observation data, black lines represent posterior estimates, and red stars (with blue dashed line) denote the SDD.

3.5. Evaluation

We evaluated snow depth (i.e., S1 observations and PBS experiments) with standard valuation metrics, including coefficient of determination (R^2), root mean squared error (RMSE), mean bias, mean absolute error (MAE), and relative mean absolute difference (RMAD). These were selected to enable comparisons to other studies (Lievens et al., 2019; Broxton et al., 2024; Hoppinen et al., 2024). To avoid seasonal inflation of R^2 in time series, where snowpack seasonality alone can yield artificially high correlations, we restrict temporal validation to dates where both modeled and observed snow depth are present (i.e., excluding summer/no-snow periods). These dates span the snow season (October 1 to April 30 or until disappearance in the SDD case), ensuring metrics evaluates on aligned timesteps. For spatial validation (e.g., S1 vs. LiDAR), metrics are computed for individual dates to avoid temporal autocorrelation effects. While R^2 is sensitive to underlying model forcings, we use it alongside RMSE, MAE, and mean bias to provide a comprehensive performance evaluation. We also evaluated MAE and RMAD, which are defined as:

$$MAE = \frac{1}{n}\sum|y_i - \hat{y}_i| \qquad \text{Equation (2)}$$

350     $RMAD = \dfrac{\frac{1}{n}\sum_{i}|y_i - y_i|}{\overline{y}}$ Equation (3)

351 where y_i is the observed value (e.g., LiDAR, SNOTEL, field data), y_i is the predicted value (e.g.,

352 PBS posterior mean), $\overline{y}$ is the mean of all observed/validation data values, and n represents the

353 total number of data points.

354 We also evaluated the probabilistic performance of the posterior ensemble simulations using the

355 Continuous Ranked Probability Score (CRPS) at 12 point-scale observation sites. CRPS is a

356 proper scoring rule that accounts for both the reliability and sharpness of probabilistic estimates

357 from ensemble simulations, with lower values indicating better performance. We use the discrete

358 form of CRPS as described by (Hersbach, 2000), which is equivalent to the continuous CDF-

359 based definition (Matheson and Winkler, 1976) when applied to finite ensemble samples.:

360   $CRPS(y_t, \{\hat{y}_{t,i}\}) = (1/N)\sum_{i=1}^{N}|\hat{y}_{t,i} - y_t| - (1/(2N^2))\sum_{i=1}^{N}\sum_{j=1}^{N}|\hat{y}_{t,i} - \hat{y}_{t,j}|$ Equation (4)

361   Where y_t is the observed snow depth (e.g., from SNOTEL) at time t, $\hat{y}_{t,i}$ is the snow depth

362 predicted by the i-th ensemble member at time t, and N is the total number of ensemble

363 members.

364 To quantify the added value of assimilation relative to the reference (open-loop) simulation, we

365 computed the CRPS Skill Score (CRPSS) following the symmetric formulation of (Cluzet et al.,

366 2022)

367      $CRPSS(E, R) = \{1 - CRPS(E)/CRPS(R), \quad if\ CRPS(E) < CRPS(R);$

368      $CRPS(R)/CRPS(E) - 1,\ otherwise\ \}$ Equation (5)

369 This formulation bounds CRPSS between [–1, 1], making it possible to directly compare and
370 average positive (improvement) and negative (degradation) values.

4. Results

4.1   Error Analysis

373 Errors in the S1 500m snow depth data were evaluated temporally at 11 SNOTEL stations and an

374 independent site (Snodgrass) from 2018–2021 and spatially relative to ASO LiDAR flights in 2018

375 and 2019. We included wet/flagged pixels in all our analyses/experiments because the removal of

379 flagged pixels resulted in performance degradation (results not shown). The results are shown in
380 Table 2.

381 **Table 2.** Average R^2, RMSE, Mean Bias, MAE, and RMAD values of **(a)** S1 against 11 SNOTEL sites and the
382 Snodgrass site. (b) S1 against ASO 50m LiDAR snow depth aggregated to 500m.

	(a) Temporal evaluation – average across all stations (m)					(b) Spatial evaluation – S1 against ASO LiDAR (m)		
Year	**2018**	**2019**	**2020**	**2021**	**Average**	**2018**	**2019**	**Average**
R^2	0.74	0.80	0.72	0.72	0.74	0.19	0.27	0.23
RMSE	0.32	0.39	0.39	0.53	0.40	0.74	0.91	0.82
Mean Bias	0.08	-0.07	0.09	0.26	0.09	-0.47	-0.26	-0.36
MAE	0.21	0.26	0.27	0.38	0.28	0.60	0.72	0.66
RMAD	0.61	0.39	0.47	0.68	0.53	0.77	0.43	0.60

383
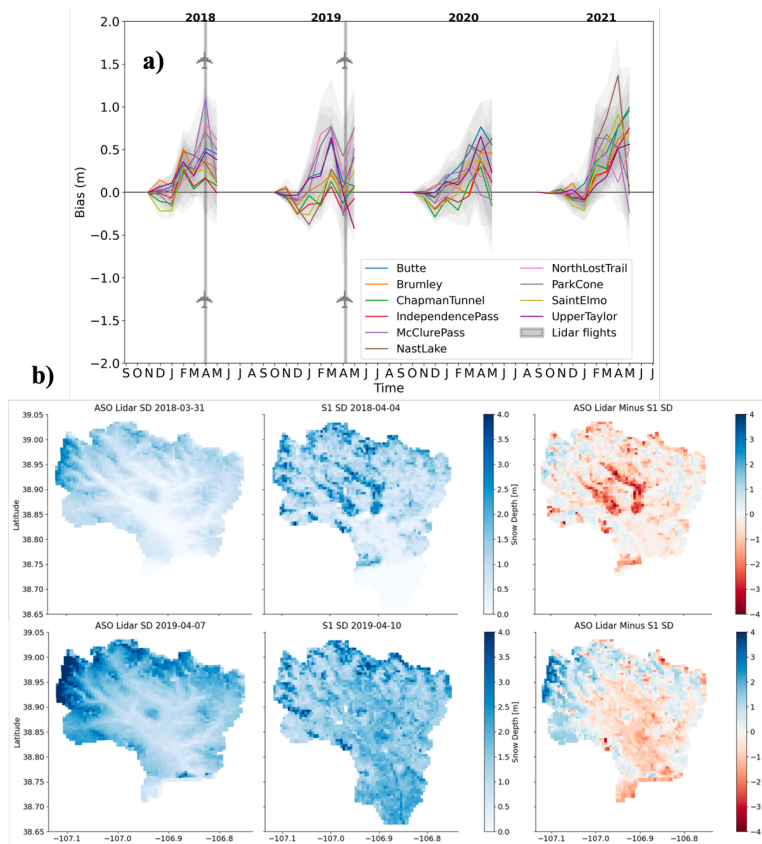
384 **Figure 4:** (a) Time-varying errors at the 11 SNOTEL sites with the timing of LiDAR flights marked with

385 thick grey lines. The solid lines represent the monthly mean bias, while the shaded region represents the ±

386 one standard deviation from the from daily bias values, indicating intra-month variability. Each station is

387 represented by a different color. (b) Comparison of ASO LiDAR and Sentinel-1–derived snow depth

388 estimates on temporally proximate dates.

389 When evaluated temporally against stations, S1 had an average bias of +0.09 m, RMSE of 0.40 m

390 and R^2 of 0.74. In contrast, when evaluated spatially against ASO, S1 had higher bias magnitude (

391 -0.36 m), a higher RMSE (0.82 m), and a lower R^2 (0.23) (Table 2). These results indicated that S1

392 performed better in capturing temporal variations compared to spatial patterns. S1 errors tended to

393   increase over time across all stations (Figure 4a), with the lowest errors in the early season and the
394   highest errors (~ 0.4m) near peak snow depth. The timing of the two LiDAR flights (Fig. 4b)
395   coincided with the time of year when errors tend to be high (thick grey vertical lines, Fig. 4a).

4.2. Temporal Experiments:

397   Before analyzing the temporal performance of our assimilation windows, we first evaluated the
398   overall skill of the posterior ensembles. We computed the CRPS (Eq. 4) across all sites and water
399   years, which directly measures the distance between ensemble predictions and observations. The
400   mean CRPS was 0.21 m, showing that posterior ensembles were, on average, within ~21 cm of
401   observed snow depth and maintained skill across a wide range of snowpack conditions (Figure S2).
402   CRPSS was then used to compare each experiment against the open-loop reference. As an
403   uncertainty-aware metric, positive CRPSS values indicate improvement relative to the reference.
404   Systematics CRPSS averages ranged from 0.08 to 0.22 (Table S2), reflecting modest but consistent
405   gains from assimilation. Higher values for SDD and joint assimilation highlight the added value
406   of snow disappearance information, while lower values for Hs-only experiments underscore the
407   noisier character of Sentinel-1 snow depth.

408   With this confidence in ensemble performance, we assessed the performance of S1 assimilation
409   with respect to window size, i.e., full window data assimilation (Hs-F) compared to the early
410   window (Hs-E) when errors were lower (Fig. 4a). The results are shown in Figure 5 for two sites:
411   (1) an independent site (Snodgrass), which was not used in the optimization of the S1 dataset, and
412   (2) a representative SNOTEL site. The time series of the two sites shows that the performance of
413   Hs-F and Hs-E is not consistent across the years. Hs-F (purple line) performed marginally better
414   than Hs-E (green line) in WY 2019 and similarly in 2020 and 2021 for the Snodgrass site. Likewise,
415   at Chapman Tunnel, Hs-F performed better than Hs-E in WY 2018, poorly in 2021, and similarly
416   to HS-E in 2019 and 2020.
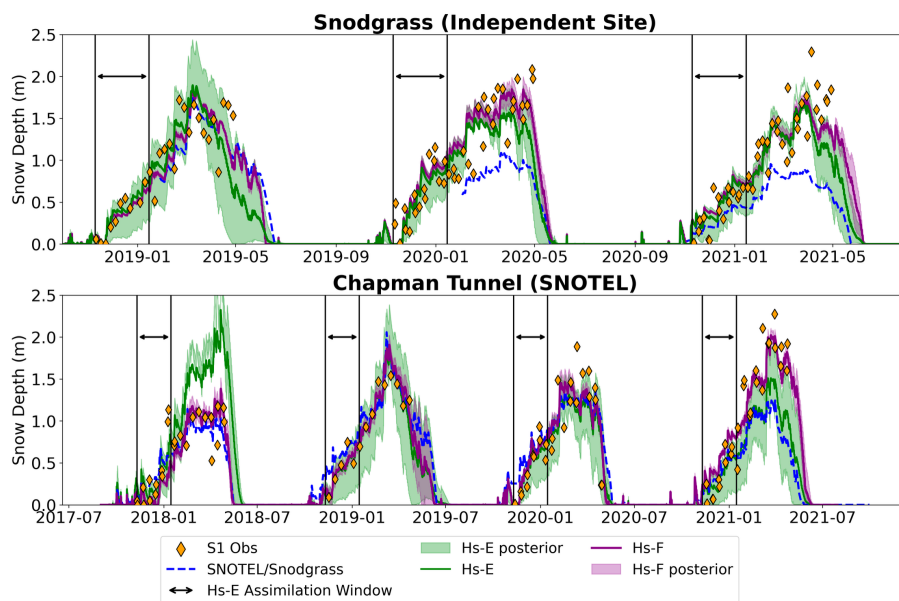
Figure 5: Temporal analysis results at (top) Snodgrass and (bottom) Chapman Tunnel. Hs-F (purple line) and Hs-E (green line) represent the posterior mean of full and early window experiments, respectively. SNOTEL and Snodgrass station data (blue dashed line) provide snow depth evaluation data. Orange diamonds represent S1 snow depth observations. Shading of respective color indicates one standard deviation of posterior particle spread, and the solid black lines represent the early assimilation window. See Figure S3 for the comparison of these experiments against the model-only run.

The statistical analysis across temporal evaluation sites give insights into the average performance of each DA window experiment. The results show RMSE of 0.29 m for Hs-F and 0.35 m for Hs-E, while R^2 is 0.88 for Hs-F and 0.86 for Hs-E (Table 3). Overall, the differences between Hs-F and Hs-E across all sites and evaluation metrics are minimal, suggesting that the accuracy of S1 snow depth retrievals remains consistent regardless of the temporal window. This implies that the retrieval method performs similarly for both the full and early windows.

Table 3: Error metrics of posterior mean of Hs-F (full window assimilation) and Hs-E (early window assimilation). Metrics are averaged across all temporal evaluation sites and across four years. See Table S2 for all experiments comparison against the model-only run.

Metrics	Experiments	
	Hs-F	Hs-E
R^2	0.88	0.86
RMSE (m)	0.29	0.35
Mean Bias (m)	0.07	0.09
MAE	0.20	0.23
RMAD	0.46	0.63

433

434 While the temporal analysis shows a marginal difference in Hs-F and Hs-E, spatial analysis reveals

435 a significant disparity in performance, with Hs-F outperforming Hs-E significantly across all

436 LiDAR flights in most metrics (Table 4). For example, Hs-F demonstrates a lower average RMSE

437 (0.66 m vs. 0.91 m), lower mean bias (0.05m vs. -0.61m) along with lower MAE (0.42m vs. 0.75m)

438 and RMAD (0.61 vs. 1.2m) compared to Hs-E. However, Hs-F performs slightly worse in specific

439 survey dates, such as R^2 on 2019-06-10, where Hs-E performs better than Hs-F (0.08 vs. 0.57m).

440 The temporal and spatial RMSE across all stations and years and LiDAR flights are shown in

441 Figure 6, with Hs-F showing lower RMSE in all cases except in the 2019-06-10 LiDAR flight.

442 Across all four LiDAR surveys, the spatial patterns in snow depth are not strongly related (i.e.,

443 $R^2<0.60$) for either Hs-E or Hs-F (Table 4, Figure 7). The density plots (Figure 7c) compare the

444 posterior mean snow depths from the full-window (Hs-F) and early-window (Hs-E) assimilation

445 experiments with LiDAR measurements. The density distribution aligns with LiDAR only in

446 certain cases (Fig. 7c), reflecting both experiments perform consistently poor relative to the LiDAR

447 snow depths. The overall analysis indicates that S1 has high errors spatially regardless of window,

448 but the full-window assimilation approach (Hs-F) provides relatively lower errors across spatial

449 locations and LiDAR dates (Figure 7). Therefore, Hs-F is utilized as the optimal window for the

450 rest of the data assimilation experiments (see Section 4.3).

451
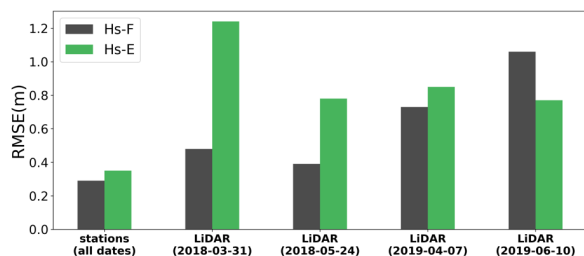
452 **Figure 6.** Bar chart comparing average RMSE from the Hs-F and Hs-E experiments when evaluated at the

453 12 snow stations. The average errors are shown for all dates and on each of the four LiDAR flight dates.

454 **Table 4.** Error metrics for the posterior mean snow depth from the Hs-F and Hs-E experiments when

455 evaluated against snow depth from four LiDAR surveys. See Table S3 for all experiments comparison

456 against the model-only run.

LiDAR Survey	Exp	R^2	RMSE (m)	Mean Bias (m)	MAE (m)	RMAD (m)
2018-03-31	Hs-F	0.51	0.48	-0.21	0.35	0.45
	Hs-E	0.29	1.24	-1.15	1.15	1.48
2018-05-24	Hs-F	0.33	0.39	0.08	0.21	0.88
	Hs-E	0.37	0.78	-0.59	0.69	2.55
2019-04-07	Hs-F	0.33	0.73	-0.08	0.52	0.31
	Hs-E	0.47	0.85	-0.52	0.66	0.40
2019-06-10	Hs-F	0.08	1.06	0.44	0.60	0.83
	Hs-E	0.57	0.77	-0.21	0.52	0.63
Average	**Hs-F**	**0.31**	**0.66**	**0.05**	**0.42**	**0.61**
	Hs-E	**0.42**	**0.91**	**-0.61**	**0.75**	**1.2**

457

458
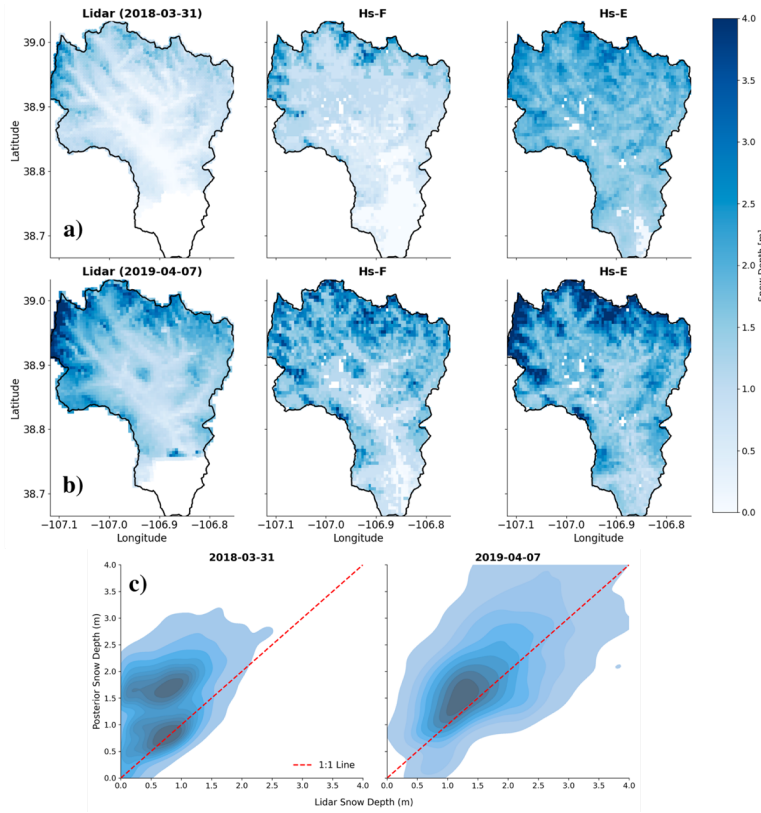
Figure 7: The first column in panels a and b shows snow depth from airborne LiDAR near peak snow
accumulation. The second and third columns in panels a and b show the posterior mean snow depth from
the Hs-F and Hs-E experiments, respectively. Panel C shows the density plot comparing two experiments
(Hs-F and Hs-E) against LiDAR measurements. Since both experiments showed similar correlations with
LiDAR, they are combined into a single plot. See Figure S5 for the experiments comparison against the
model-only run.

4.3. Joint Assimilation Experiments:

Finally, we evaluate the joint assimilation of SDD+Hs-F against SDD alone (baseline) to test the
utility of S1 snow depth for adding new information to a DA system. We utilized Hs-F instead of
Hs-E because errors tended to be lower with Hs-F (see section 4.2). The temporal results of

469   experiments 3 and 4 of the most representative and independent site are shown in Figure 8. The
470   results show that the performance of Hs-F (experiment 1), SDD+Hs-F (experiment 3), and SDD
471   alone (experiment 4) varies across the years. Hs-F performed better than SDD-Hs-F and SDD in
472   WY 2019 and 2020 and similarly in 2021 for the Snodgrass site. In the SNOTEL representative
473   site, SDD performed better or similar as Hs-F and SDD+Hs-F in all WYs. The temporal analysis
474   indicates that joint assimilation and SDD alone experiments perform better than Hs-F minimally
475   across all metrics (~0.01m). However, the performance of SDD+Hs-F is approximately the same
476   as the baseline SDD experiment (Table 5), suggesting that joint assimilation of SDD with S1 snow
477   depth does not significantly enhance performance relative to just assimilating SDD alone.

Commented [MR1]: ? Missing word here?

478
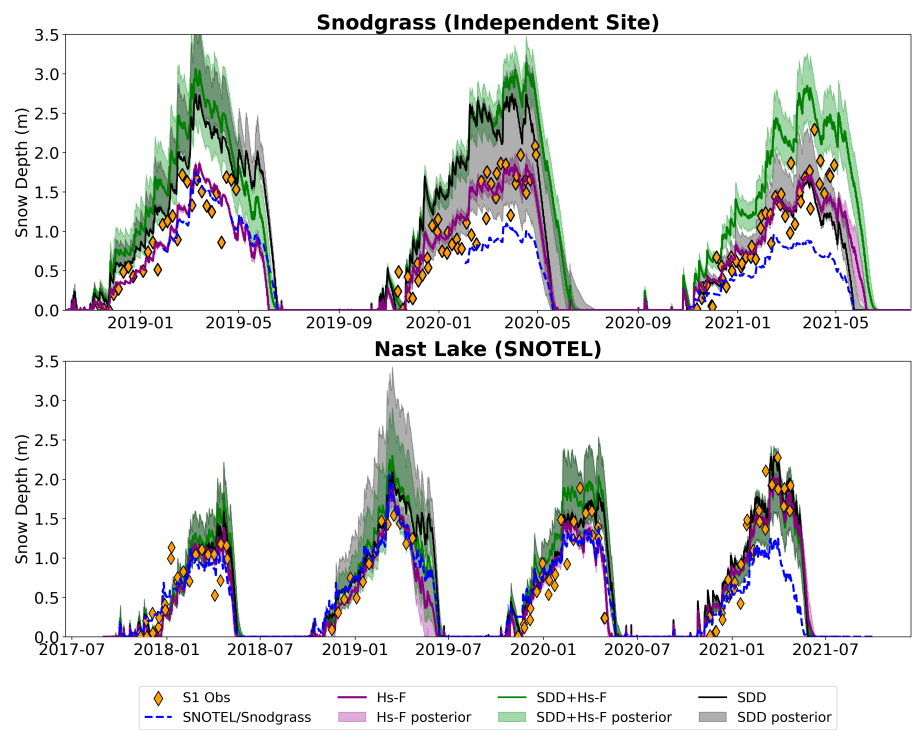
Figure 8: Example results of the joint assimilation experiments at (a) Snodgrass and (b) Nast Lake. Hs-F
480   (purple line) and SDD+Hs-F (green line) represent the posterior mean for each experiment. SDD (black
481   line) is the posterior snow depth based on assimilating only SDD. SNOTEL and Snodgrass in situ (blue
482   dashed line) provide snow depth evaluation data. Orange diamonds represent S1 snow depth observations.

483 Shading of respective color indicates one standard deviation of posterior particle spread. See Figure S4 for

484 the comparison against the model-only run.

485 **Table 5.** Error metrics of the posterior mean of Hs-F (full window assimilation), SDD+HS-F (joint

486 assimilation), and SDD. Metrics are averaged across all temporal evaluation sites and across four years. See

487 Table S2 for all experiments comparison against the model-only run.

Metrics	Experiments	
	SDD+Hs-F	SDD
R^2	0.92	0.89
RMSE	0.28	0.28
Mean Bias	0.15	0.14
MAE	0.19	0.19
RMAD	0.42	0.48

488
489
490
491
492

493 Spatial analysis provides more insights on univariate (Hs-F or SDD) and joint assimilation

494 experiments (Hs-F+SDD). Across all metrics, assimilating SDD alone results in higher spatial

495 performance compared to both Hs-F and SDD+Hs-F. The temporal and spatial RMSE across all

496 stations, years, and LiDAR flights are shown in Figure 9. The RMSE is 0.41 m for SDD

497 assimilation averaged across all LiDAR flights and years, which is lower than the RMSE of Hs-F

498 (0.66 m, Table 4) and SDD+Hs-F (0.70 m, Table 6). Additionally, assimilating SDD alone

499 demonstrates a stronger relationship with LiDAR observations ($R^2 = 0.72$) compared to Hs-F (R^2

500 $= 0.31$) and SDD+Hs-F ($R^2 = 0.46$), with better spatial pattern alignment across both LiDAR dates

501 near peak accumulation (Table 6, Fig. 10). Joint assimilation (SDD+Hs-F) shows lower

502 performance in comparison to Hs-F alone or SDD alone, suggesting that the combination of S1

503 with SDD does not enhance performance and may potentially degrade it.

504
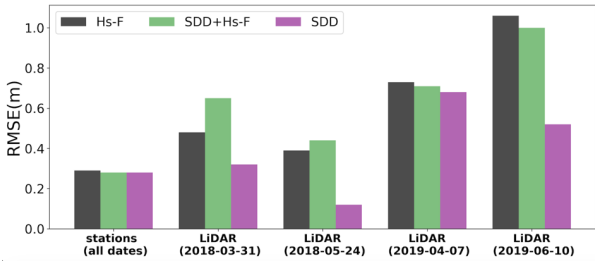
505 **Figure 9:** Bar chart comparing RMSE for Hs-F, SDD+Hs-F, and SDD experiments of stations

506 (SNOTEL+Snodgrass) averaged across all stations and all four years, and each LiDAR flight.

507
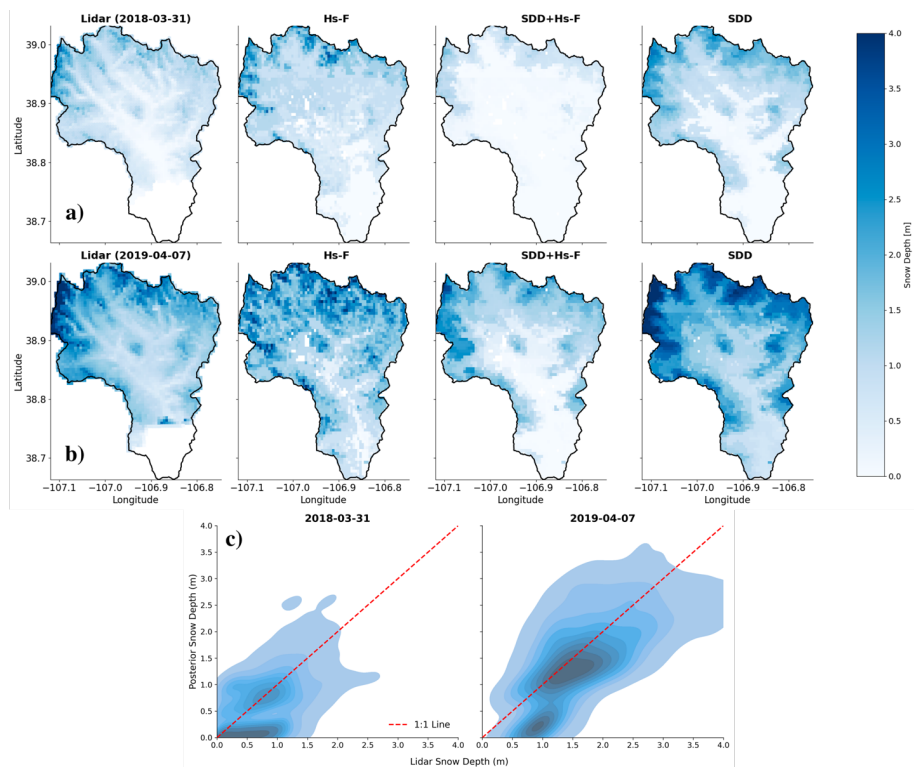
Figure 10: The first column in panels a and b shows snow depth from airborne LiDAR near peak snow

accumulation. The second, third, and fourth columns in panels a and b show the posterior mean snow depth

from the Hs-F, SDD+Hs-F, and SDD experiments, respectively. Panel c shows the density plot comparing

three experiments (Hs-F, SDD-Hs-F, and SDD) against LiDAR measurements. Since both experiments

showed similar correlations (or better in the case of SDD) with LiDAR, they are combined into a single

plot. See Figure S5 for the comparison against the model-only run

Table 6. Error metrics of posterior mean snow depth from the Hs-F, SDD+Hs-F, and SDD experiments
when evaluated against four LiDAR surveys. See Table S3 for the comparison against the model-only run.

LiDAR Survey	Exp	R^2	RMSE (m)	Mean Bias (m)	MAE (m)	RMAD (m)
2018-03-31	Hs-F	0.51	0.48	-0.21	0.35	0.45
	SDD+Hs-F	0.58	0.65	0.55	0.55	0.71

	SDD	0.74	0.32	-0.25	0.33	0.42
2018-04-24	Hs-F	0.33	0.39	0.08	0.21	0.88
	SDD+Hs-F	0.10	0.44	0.23	0.23	0.99
	SDD	0.70	0.12	-0.01	0.13	0.53
2019-04-07	Hs-F	0.33	0.73	-0.08	0.52	0.31
	SDD+Hs-F	0.69	0.71	0.55	0.62	0.35
	SDD	0.70	0.68	-0.48	0.54	0.32
2019-06-10	Hs-F	0.08	1.06	0.44	0.60	0.83
	SDD+Hs-F	0.49	1.0	0.71	0.71	0.85
	SDD	0.76	0.52	-0.09	0.34	0.40
Average	**Hs-F**	**0.31**	**0.66**	**0.05**	**0.42**	**0.61**
	SDD+Hs-F	**0.46**	**0.70**	**0.51**	**0.52**	**0.72**
	SDD	**0.72**	**0.41**	**0.20**	**0.33**	**0.42**

5. Discussion

This study evaluates the utility of S1 SAR-derived snow depth data in the mountainous ERB (Colorado) to support spatiotemporal snow depth mapping within a DA framework. Our analysis highlights inconsistencies in temporal versus spatial errors in S1 snow depth data. While S1 demonstrates lower temporal errors (RMSE = 0.40 m, R^2 = 0.74), spatial errors were higher (RMSE = 0.82m, R^2 = 0.23) relative to LiDAR flights near or after peak accumulation (Table 2). Temporal errors were lower during the early season but increased over time, particularly during the ablation phase when wet snow conditions become more likely (Figure 4). These discrepancies align with prior studies (Broxton et al., 2024; Hoppinen et al., 2024), which report significant errors in S1 snow depth data under wet snow conditions and poor spatial correlations with airborne LiDAR data (RMSE > 0.7 m, R^2 < 0.3). The limitation may also stem from the timing of spatial validation data, as most LiDAR flights are conducted near or after peak snow depth when S1 performance is most likely compromised due to wet snow. However, early-season (Hs-E) experiments show high uncertainty, suggesting uncertainty is likely due to noisy observations without a clear error pattern. Unlike prior studies that proposed excluding flagged wet pixels as a mitigation strategy, we found that removing flagged pixels increased errors, potentially due to the omission of shallow dry snow observations (Hoppinen et al., 2024). Lievens et al. (2022) reported significantly lower errors (~0.25 m) in the European Alps, which is contrary to studies (Broxton

534 et al., 2024; Hoppinen et al., 2024) focused on the Western US, including our study in the ERB.

535 The lower errors reported by Lievens et al. (2022) could be due to a higher overpass frequency

536 and denser validation datasets and needs further investigation. Therefore, while S1 may be useful

537 in other regions, our findings emphasize its limited reliability in much of the Western US.,

538 including ERB, and caution against broad generalizations.

539 Noisy observations are not inherently problematic for data assimilation, provided their uncertainty

540 is well characterized. Our analysis showed errors increasing with time and did not reveal consistent

541 spatial or year-to-year error patterns, limiting the development of sophisticated error models

542 (Figure 4). For simplicity, we treated observational errors as time-invariant for the PBS

543 assimilation, but we acknowledge that it is possible to include dynamic errors in DA; this is most

544 straightforward for sequential DA approaches like the particle filter (PF). To assess the potential

545 benefit of a dynamic error formulation for handling time-varying uncertainty, we compared the

546 PBS with constant observation error against PF implementations using constant (PFcons) versus

547 dynamic (PFvar) errors (Figure S1, Table S1). The results showed limited improvement (< 0.040

548 m MAE). This is consistent with Dunmire et al. (2025), who also tested variable observation errors

549 when assimilating S1 with an Ensemble Kalman Filter and found that it improved MAE by ~0.025

550 m at roughly half of their evaluation sites across the European Alps, where Sentinel-1 retrievals

551 have better performance (Lievens et al., 2022). Given these modest impacts on performance for

552 sequential DA approaches, we assume our use of a constant observation error did not significantly

553 impact our results with the PBS, though future work is needed to further confirm this assumption.

554 We developed our DA experiments based on recommendations by Gascoin et al. (2024), and aimed

555 to determine the optimal assimilation window (full season vs. early season) with lower uncertainty

556 for generating spatiotemporal snow depth maps. The comparison between the full-window (Hs-F)

557 and early-window (Hs-E) approaches showed minimal improvement in error metrics in the

558 temporal analysis at ground-based stations. Spatial evaluations against LiDAR data resulted in Hs-

559 F performing better than Hs-E. However, Hs-F increases the likelihood of including wet snow

560 conditions and higher errors later in the snow season. The early-window approach benefits from

561 reduced retrieval errors due to its focus on lower snow depth values and assumed higher likelihood

562 of dry snow in December and January. However, this approach is more effective in regions where

563 a significant fraction of the total SWE accumulates early in the season (Lundquist et al., 2023). In

591   contrast, basins like the ERB receive significant snowfall after January, which reduces the early-
592   season window's ability to predict SWE reliably later in the year (e.g., April-onward). This seasonal
593   snow accumulation pattern likely explains why the early-window approach is less effective in our
594   study. This variability underscores the inherent challenges in using early-season conditions to make
595   broader inferences about snowpack dynamics later in the year. Despite these limitations, the results
596   show that errors in S1 snow depth retrievals are relatively independent of the assimilation window
597   in the ERB.

598   The joint assimilation of S1 snow depth with SDD was conducted to understand what information
599   is added by S1 and to test whether SDD can provide additional constraints on the DA outcome.
600   Previous studies successfully used joint assimilation in a DA system with satellite data such as
601   ICESat-2 (Mazzolini et al., 2024). However, joint assimilation showed limited value with S1 snow
602   depth data: The errors did not decrease when assimilating S1 depth with SDD. Assimilating SDD
603   alone showed a higher R^2 value and lower errors on average compared to Hs-F and SDD+Hs-F.

604   There are some caveats and potential limitations in the study. The study did not utilize downscaling
605   before assimilation; however, we did not see extreme bias in reference runs (model only, Figure
606   S3-5), which suggests that limited gains from DA are primarily due to S1 observation uncertainty,
607   rather than a lack of downscaling. Additionally, recent research has shown that assimilation of S1
608   snow depth can implicitly be used as downscaling (Bachand et al., 2025). The current study
609   focused on a single basin and a limited number of nearby snow pillow stations over a four-year
610   period. A more comprehensive evaluation against LiDAR data has already been conducted with
611   the available LiDAR data in the western U.S. (Broxton et al., 2024; Hoppinen et al., 2024). Similar
612   to previous studies, we were also limited by the evaluation of LiDAR data since it was only
613   available at peak snow depth or in the melt season, when S1 has higher errors. This highlights the
614   importance of expanding the spatial and temporal coverage of evaluation data.

615   Future research should continue to develop and explore approaches for using Sentinel-1 and other
616   spaceborne remote sensing platforms for mapping SWE and other related snowpack variables. One
617   established capability of S1 backscatter data is for wet snow mapping (Cluzet et al., 2024; Gagliano
618   et al., 2023; Nagler et al., 2016). For snow depth and SWE mapping, the existing Lievens et al.
619   (2019) algorithm may be improved through corrections with machine learning as proposed by

620 Broxton et al. (2024). Alternatively, interferometric SAR (InSAR) techniques (Oveisgharan et al.,
621 2024) have recently been shown to have some potential for mapping SWE with S1 C-band data,
622 although challenges related to the frequency of satellite passes remain a challenge (Deeb et al.,
623 2011) and these techniques are likely more reliable with L-band SAR data. The upcoming NISAR
624 mission will provide L-band SAR data, which may provide new opportunities for accurate snow
625 depth mapping in mountainous regions that may overcome some of the current limitations of C-
626 band SAR. However, other limitations may persist for NISAR (e.g., wet snow).

6. Conclusion

628 This study underscores the challenges of using C-Band S1 SAR-derived snow depth data within a
629 DA framework. While S1 is currently the only high-resolution (<1 km) remotely sensed snow
630 depth dataset available across the Northern Hemisphere, it demonstrated notable biases and
631 limitations in snow depth mapping in the East River Basin in the western U.S. These errors were
632 similar across both full-window and early-window assimilation experiments and align with prior
633 studies that reported significant spatial biases and retrieval errors. Importantly, we did not observe
634 a consistent seasonal or interannual pattern in the errors, which limits the development of robust
635 correction or error models. The joint assimilation of S1 snow depth with SDD data showed limited
636 or no improvement, suggesting that assimilating SDD alone yields greater accuracy.

637 While recognizing that our study focused on a single mountain basin, we conclude that the
638 reliability of the current S1 snow depth retrieval algorithm presents major challenges for a snow
639 DA system. Future research should prioritize algorithm improvements, explore machine learning
640 techniques, and conduct additional testing across a wider range of basins and with spatial data.
641 Enhanced methods for snow depth monitoring would improve understanding of snowpack
642 dynamics in regions where ground-based observations are sparse or unavailable, supporting better
643 water resource management and climate impact assessments.

644

645 **Author Contributions:** Data curation and Analysis: BM. Experiment Design: BM, MR, EE.
646 Writing: The draft was led by BM with key contribution and editing by all co-authors. Funding
647 Acquisition: MR and ES.

648 **Code and data availability:** This study used airborne LiDAR snow depth data (ASO, Inc.),
649 MODIS and ERA5 data (GEE), NRCS SNOTEL, and independent validation data from teams at
650 the University of Colorado and Oregon State University. The MuSA code, which integrates
651 FSM, is available at https://github.com/ealonsogzl/MuSA, with FSM originally developed by
652 Richard Essery. Computational resources were provided by Oregon State University's College of
653 Engineering.

654

655 **Competing interests:** The authors declare that they have no conflict of interest.

656

657 **Acknowledgments**

658 This work was supported by the National Aeronautics and Space Administration (NASA)
659 Terrestrial Hydrology Program under Award No. 80NSSC22K0685. The authors thank Esteban
660 Alonso González for making the MuSA code available (https://github.com/ealonsogzl/MuSA) and
661 Richard Essery for development of FSM. This work utilized resources from Oregon State
662 University College of Engineering high-performance computing network. The independent
663 temporal validation data was collected by student teams from the University of Colorado (Eric
664 Small Hydrology Group) and Oregon State University (CryoSphere Interactions and Geospatial
665 Hydrology Team). The authors also thank the ASO, Inc. team for providing the airborne LiDAR
666 snow depth and GEE for facilitating the access of MODIS and meteorological forcing data used
667 in the study.

668

669 **References:**

670 Aalstad, K., Westermann, S., and Bertino, L.: Evaluating satellite retrieved fractional snow-
671 covered area at a high-Arctic site using terrestrial photography, Remote Sensing of
672 Environment, 239, 111618, https://doi.org/10.1016/j.rse.2019.111618, 2020.

673 Alonso-González, E., Aalstad, K., Baba, M. W., Revuelto, J., López-Moreno, J. I., Fiddes, J.,
674 Essery, R., and Gascoin, S.: The Multiple Snow Data Assimilation System (MuSA v1.0),
675 Geosci. Model Dev., 15, 9127–9155, https://doi.org/10.5194/gmd-15-9127-2022, 2022.

676 Bachand, C. L., Andrews, L. C., Rouf, T., and Girotto, M.: The Utility of Satellite Snow Depth
677 Observations for Downscaling Hydrologic Variables over the Indus Basin Mountain Ranges,
678 Journal of Hydrometeorology, 26, 555–575, https://doi.org/10.1175/JHM-D-24-0131.1,
679 2025.

680 Barnett, T. P., Adam, J. C., and Lettenmaier, D. P.: Potential impacts of a warming climate on
681 water availability in snow-dominated regions, Nature, 438, 303–309,
682 https://doi.org/10.1038/nature04141, 2005.

683 Besso, H., Shean, D., and Lundquist, J. D.: Mountain snow depth retrievals from
684 customized processing of ICESat-2 satellite laser altimetry, Remote Sensing of
685 Environment, 300, 113843, https://doi.org/10.1016/j.rse.2023.113843, 2024.

686 Bonner, H. M., Smyth, E., Raleigh, M. S., and Small, E. E.: A Meteorology and Snow Data Set
687 From Adjacent Forested and Meadow Sites at Crested Butte, CO, USA, Water Resources
688 Research, 58, https://doi.org/10.1029/2022WR033006, 2022.

689 Brangers, I., Lievens, H., Getirana, A., and De Lannoy, G. J. M.: Sentinel-1 Snow Depth
690 Assimilation to Improve River Discharge Estimates in the Western European Alps, Water
691 Resources Research, 60, e2023WR035019, https://doi.org/10.1029/2023WR035019, 2024.

692 Broxton, P., Ehsani, M. R., and Behrangi, A.: Improving Mountain Snowpack Estimation
693 Using Machine Learning With Sentinel-1, the Airborne Snow Observatory, and University of
694 Arizona Snowpack Data, Earth and Space Science, 11, e2023EA002964,
695 https://doi.org/10.1029/2023EA002964, 2024.

696 Broxton, P. D., Van Leeuwen, W. J. D., and Biederman, J. A.: Improving Snow Water
697 Equivalent Maps With Machine Learning of Snow Survey and Lidar Measurements, Water
698 Resources Research, 55, 3739–3757, https://doi.org/10.1029/2018WR024146, 2019.

699 Chang, A. T. C., Foster, J. L., and Hall, D. K.: Nimbus-7 SMMR Derived Global Snow Cover
700 Parameters, A. Glaciology., 9, 39–44, https://doi.org/10.3189/S0260305500200736, 1987.

701 Clark, M. P., Hendrikx, J., Slater, A. G., Kavetski, D., Anderson, B., Cullen, N. J., Kerr, T., Örn
702 Hreinsson, E., and Woods, R. A.: Representing spatial variability of snow water equivalent

in hydrologic and land-surface models: A review, Water Resources Research, 47, 2011WR010745, https://doi.org/10.1029/2011WR010745, 2011.

Cluzet, B., Lafaysse, M., Deschamps-Berger, C., Vernay, M., and Dumont, M.: Propagating information from snow observations with CrocO ensemble data assimilation system: a 10-years case study over a snow depth observation network, The Cryosphere, 16, 1281–1298, https://doi.org/10.5194/tc-16-1281-2022, 2022.

Cluzet, B., Magnusson, J., Quéno, L., Mazzotti, G., Mott, R., and Jonas, T.: Exploring how Sentinel-1 wet-snow maps can inform fully distributed physically based snowpack models, The Cryosphere, 18, 5753–5767, https://doi.org/10.5194/tc-18-5753-2024, 2024.

Copernicus Climate Change Service: ERA5-Land hourly data from 1950 to present, https://doi.org/10.24381/CDS.E2161BAC, 2019.

Crumley, R. L., Palomaki, R. T., Nolin, A. W., Sproles, E. A., and Mar, E. J.: SnowCloudMetrics: Snow Information for Everyone, Remote Sensing, 12, 3341, https://doi.org/10.3390/rs12203341, 2020.

Daly, C., Neilson, R. P., and Phillips, D. L.: A Statistical-Topographic Model for Mapping Climatological Precipitation over Mountainous Terrain, J. Appl. Meteor., 33, 140–158, https://doi.org/10.1175/1520-0450(1994)033%253C0140:ASTMFM%253E2.0.CO;2, 1994.

De Boer, G., White, A., Cifelli, R., Intrieri, J., Rose Abel, M., Mahoney, K., Meyers, T., Lantz, K., Hamilton, J., Currier, W., Sedlar, J., Cox, C., Hulm, E., Riihimaki, L. D., Adler, B., Bianco, L., Morales, A., Wilczak, J., Elston, J., Stachura, M., Jackson, D., Morris, S., Chandrasekar, V., Biswas, S., Schmatz, B., Junyent, F., Reithel, J., Smith, E., Schloesser, K., Kochendorfer, J., Meyers, M., Gallagher, M., Longenecker, J., Olheiser, C., Byteway, J., Moore, B., Calmer, R., Shupe, M. D., Butterworth, B., Heflin, S., Palladino, R., Feldman, D., Williams, K., Pinto, J., Osborn, J., Costa, D., Hall, E., Herrera, C., Hodges, G., Soldo, L., Stierle, S., and Webb, R. S.: Supporting Advancement in Weather and Water Prediction in the Upper Colorado River Basin: The SPLASH Campaign, Bulletin of the American Meteorological Society, 104, E1853–E1874, https://doi.org/10.1175/BAMS-D-22-0147.1, 2023.

De Lannoy, G. J. M., Bechtold, M., Busschaert, L., Heyvaert, Z., Modanesi, S., Dunmire, D., Lievens, H., Getirana, A., and Massari, C.: Contributions of Irrigation Modeling, Soil Moisture and Snow Data Assimilation to High-Resolution Water Budget Estimates Over the Po Basin: Progress Towards Digital Replicas, J Adv Model Earth Syst, 16, https://doi.org/10.1029/2024ms004433, 2024.

Deeb, E. J., Forster, R. R., and Kane, D. L.: Monitoring snowpack evolution using interferometric synthetic aperture radar on the North Slope of Alaska, USA, International Journal of Remote Sensing, 32, 3985–4003, https://doi.org/10.1080/01431161003801351, 2011.

739 Derksen, C., Walker, A., and Goodison, B.: Evaluation of passive microwave snow water
740 equivalent retrievals across the boreal forest/tundra transition of western Canada, Remote
741 Sensing of Environment, 96, 315–327, https://doi.org/10.1016/j.rse.2005.02.014, 2005.

742 Deschamps-Berger, C., Cluzet, B., Dumont, M., Lafaysse, M., Berthier, E., Fanise, P., and
743 Gascoin, S.: Improving the Spatial Distribution of Snow Cover Simulations by Assimilation
744 of Satellite Stereoscopic Imagery, Water Resources Research, 58,
745 https://doi.org/10.1029/2021WR030271, 2022.

746 Deschamps-Berger, C., Gascoin, S., Shean, D., Besso, H., Guiot, A., and López-Moreno, J.
747 I.: Evaluation of snow depth retrievals from ICESat-2 using airborne laser-scanning data,
748 The Cryosphere, 17, 2779–2792, https://doi.org/10.5194/tc-17-2779-2023, 2023.

749 Dozier, J.: Mountain hydrology, snow color, and the fourth paradigm, EoS Transactions, 92,
750 373–374, https://doi.org/10.1029/2011EO430001, 2011.

751 Dozier, J., Bair, E. H., and Davis, R. E.: Estimating the spatial distribution of snow water
752 equivalent in the world's mountains, WIREs Water, 3, 461–474,
753 https://doi.org/10.1002/wat2.1140, 2016.

754 Dunmire, D., Lievens, H., Boeykens, L., and De Lannoy, G. J. M.: A machine learning
755 approach for estimating snow depth across the European Alps from Sentinel-1 imagery,
756 Remote Sensing of Environment, 314, 114369, https://doi.org/10.1016/j.rse.2024.114369,
757 2024.

758 Dunmire, D., Bechtold, M., Boeykens, L., and De Lannoy, G. J. M.: Advancing snow data
759 assimilation with a dynamic observation uncertainty, https://doi.org/10.5194/egusphere-
760 2025-2306, 28 May 2025.

761 Elder, K., Rosenthal, W., and Davis, R. E.: Estimating the spatial distribution of snow water
762 equivalence in a montane watershed, Hydrol. Process., 12, 1793–1808,
763 https://doi.org/10.1002/(SICI)1099-1085(199808/09)12:10/11%253C1793::AID-
764 HYP695%253E3.0.CO;2-K, 1998.

765 Essery, R.: A factorial snowpack model (FSM 1.0), Geosci. Model Dev., 8, 3867–3876,
766 https://doi.org/10.5194/gmd-8-3867-2015, 2015.

767 Essery, R., Mazzotti, G., Barr, S., Jonas, T., Quaife, T., and Rutter, N.: A Flexible Snow Model
768 (FSM 2.1.0) including a forest canopy, https://doi.org/10.5194/egusphere-2024-2546, 11
769 October 2024.

770 Feldman, D. R., Aiken, A. C., Boos, W. R., Carroll, R. W. H., Chandrasekar, V., Collis, S.,
771 Creamean, J. M., De Boer, G., Deems, J., DeMott, P. J., Fan, J., Flores, A. N., Gochis, D.,
772 Grover, M., Hill, T. C. J., Hodshire, A., Hulm, E., Hume, C. C., Jackson, R., Junyent, F.,
773 Kennedy, A., Kumjian, M., Levin, E. J. T., Lundquist, J. D., O'Brien, J., Raleigh, M. S., Reithel,
774 J., Rhoades, A., Rittger, K., Rudisill, W., Sherman, Z., Siirila-Woodburn, E., Skiles, S. M.,

775 Smith, J. N., Sullivan, R. C., Theisen, A., Tuftedal, M., Varble, A. C., Wiedlea, A., Wielandt,
776 S., Williams, K., and Xu, Z.: The Surface Atmosphere Integrated Field Laboratory (SAIL)
777 Campaign, Bulletin of the American Meteorological Society, 104, E2192–E2222,
778 https://doi.org/10.1175/BAMS-D-22-0049.1, 2023.

779 Foster, J., Liston, G., Koster, R., Essery, R., Behr, H., Dumenil, L., Verseghy, D., Thompson,
780 S., Pollard, D., and Cohen, J.: Snow Cover and Snow Mass Intercomparisons of General
781 Circulation Models and Remotely Sensed Datasets, J. Climate, 9, 409–426,
782 https://doi.org/10.1175/1520-0442(1996)009%253C0409:SCASMI%253E2.0.CO;2, 1996.

783 Gagliano, E., Shean, D., Henderson, S., and Vanderwilt, S.: Capturing the Onset of
784 Mountain Snowmelt Runoff Using Satellite Synthetic Aperture Radar, Geophysical
785 Research Letters, 50, e2023GL105303, https://doi.org/10.1029/2023GL105303, 2023.

786 Girotto, M., Musselman, K. N., and Essery, R. L. H.: Data Assimilation Improves Estimates
787 of Climate-Sensitive Seasonal Snow, Curr Clim Change Rep, 6, 81–94,
788 https://doi.org/10.1007/s40641-020-00159-7, 2020.

789 Girotto, M., Formetta, G., Azimi, S., Bachand, C., Cowherd, M., De Lannoy, G., Lievens, H.,
790 Modanesi, S., Raleigh, M. S., Rigon, R., and Massari, C.: Identifying snowfall elevation
791 patterns by assimilating satellite-based snow depth retrievals, Science of The Total
792 Environment, 906, 167312, https://doi.org/10.1016/j.scitotenv.2023.167312, 2024.

793 Grünewald, T., Schirmer, M., Mott, R., and Lehning, M.: Spatial and temporal variability of
794 snow depth and ablation rates in a small mountain catchment, The Cryosphere, 4, 215–
795 225, https://doi.org/10.5194/tc-4-215-2010, 2010.

796 Herbert, J. N., Raleigh, M. S., and Small, E. E.: Reanalyzing the spatial representativeness of
797 snow depth at automated monitoring stations using airborne lidar data, The Cryosphere,
798 18, 3495–3512, https://doi.org/10.5194/tc-18-3495-2024, 2024.

799 Hersbach, H.: Decomposition of the Continuous Ranked Probability Score for Ensemble
800 Prediction Systems, Wea. Forecasting, 15, 559–570, https://doi.org/10.1175/1520-
801 0434(2000)015%253C0559:dotcrp%253E2.0.co;2, 2000.

802 Hersbach, H., Bell, B., Berrisford, P., Hirahara, S., Horányi, A., Muñoz-Sabater, J., Nicolas,
803 J., Peubey, C., Radu, R., Schepers, D., Simmons, A., Soci, C., Abdalla, S., Abellan, X.,
804 Balsamo, G., Bechtold, P., Biavati, G., Bidlot, J., Bonavita, M., De Chiara, G., Dahlgren, P.,
805 Dee, D., Diamantakis, M., Dragani, R., Flemming, J., Forbes, R., Fuentes, M., Geer, A.,
806 Haimberger, L., Healy, S., Hogan, R. J., Hólm, E., Janisková, M., Keeley, S., Laloyaux, P.,
807 Lopez, P., Lupu, C., Radnoti, G., De Rosnay, P., Rozum, I., Vamborg, F., Villaume, S., and
808 Thépaut, J.: The ERA5 global reanalysis, Quart J Royal Meteoro Soc, 146, 1999–2049,
809 https://doi.org/10.1002/qj.3803, 2020.

810   Hoppinen, Z., Palomaki, R. T., Brencher, G., Dunmire, D., Gagliano, E., Marziliano, A.,
811   Tarricone, J., and Marshall, H.-P.: Evaluating snow depth retrievals from Sentinel-1 volume
812   scattering over NASA SnowEx sites, The Cryosphere, 18, 5407–5430,
813   https://doi.org/10.5194/tc-18-5407-2024, 2024.

814   Hu, Y., Lu, X., Zeng, X., Stamnes, S. A., Neuman, T. A., Kurtz, N. T., Zhai, P., Gao, M., Sun, W.,
815   Xu, K., Liu, Z., Omar, A. H., Baize, R. R., Rogers, L. J., Mitchell, B. O., Stamnes, K., Huang, Y.,
816   Chen, N., Weimer, C., Lee, J., and Fair, Z.: Deriving Snow Depth From ICESat-2 Lidar
817   Multiple Scattering Measurements, Front. Remote Sens., 3, 855159,
818   https://doi.org/10.3389/frsen.2022.855159, 2022.

819   Hubbard, S. S., Williams, K. H., Agarwal, D., Banfield, J., Beller, H., Bouskill, N., Brodie, E.,
820   Carroll, R., Dafflon, B., Dwivedi, D., Falco, N., Faybishenko, B., Maxwell, R., Nico, P.,
821   Steefel, C., Steltzer, H., Tokunaga, T., Tran, P. A., Wainwright, H., and Varadharajan, C.: The
822   East River, Colorado, Watershed: A Mountainous Community Testbed for Improving
823   Predictive Understanding of Multiscale Hydrological–Biogeochemical Dynamics, Vadose
824   Zone Journal, 17, 1–25, https://doi.org/10.2136/vzj2018.03.0061, 2018.

825   Jarvis, A., Guevara, E., Reuter, H. I., and Nelson, A. D.: Hole-filled SRTM for the globe :
826   version 4 : data grid, 2008.

827   Kelly, R. E., Chang, A. T., Tsang, L., and Foster, J. L.: A prototype AMSR-E global snow area
828   and snow depth algorithm, IEEE Trans. Geosci. Remote Sensing, 41, 230–242,
829   https://doi.org/10.1109/TGRS.2003.809118, 2003.

830   Kinar, N. J. and Pomeroy, J. W.: Measurement of the physical properties of the snowpack,
831   Reviews of Geophysics, 53, 481–544, https://doi.org/10.1002/2015RG000481, 2015.

832   Largeron, C., Dumont, M., Morin, S., Boone, A., Lafaysse, M., Metref, S., Cosme, E., Jonas,
833   T., Winstral, A., and Margulis, S. A.: Toward Snow Cover Estimation in Mountainous Areas
834   Using Modern Data Assimilation Methods: A Review, Front. Earth Sci., 8, 325,
835   https://doi.org/10.3389/feart.2020.00325, 2020.

836   Lievens, H., Demuzere, M., Marshall, H.-P., Reichle, R. H., Brucker, L., Brangers, I., De
837   Rosnay, P., Dumont, M., Girotto, M., Immerzeel, W. W., Jonas, T., Kim, E. J., Koch, I., Marty,
838   C., Saloranta, T., Schöber, J., and De Lannoy, G. J. M.: Snow depth variability in the Northern
839   Hemisphere mountains observed from space, Nat Commun, 10, 4629,
840   https://doi.org/10.1038/s41467-019-12566-y, 2019.

841   Lievens, H., Brangers, I., Marshall, H.-P., Jonas, T., Olefs, M., and De Lannoy, G.: Sentinel-1
842   snow depth retrieval at sub-kilometer resolution over the European Alps, The Cryosphere,
843   16, 159–177, https://doi.org/10.5194/tc-16-159-2022, 2022.

844 López-Moreno, J. I., Fassnacht, S. R., Beguería, S., and Latron, J. B. P.: Variability of snow
845 depth at the plot scale: implications for mean depth estimation and sampling strategies,
846 The Cryosphere, 5, 617–629, https://doi.org/10.5194/tc-5-617-2011, 2011.

847 Lundquist, J. D., Kim, R. S., Durand, M., and Prugh, L. R.: Seasonal Peak Snow Predictability
848 Derived From Early-Season Snow in North America, Geophysical Research Letters, 50,
849 e2023GL103802, https://doi.org/10.1029/2023GL103802, 2023.

850 Luojus, K., Pulliainen, J., Takala, M., Lemmetyinen, J., Mortimer, C., Derksen, C., Mudryk, L.,
851 Moisander, M., Hiltunen, M., Smolander, T., Ikonen, J., Cohen, J., Salminen, M., Norberg, J.,
852 Veijola, K., and Venäläinen, P.: GlobSnow v3.0 Northern Hemisphere snow water
853 equivalent dataset, Sci Data, 8, 163, https://doi.org/10.1038/s41597-021-00939-2, 2021.

854 Margulis, S. A., Girotto, M., Cortés, G., and Durand, M.: A Particle Batch Smoother
855 Approach to Snow Water Equivalent Estimation, Journal of Hydrometeorology, 16, 1752–
856 1772, https://doi.org/10.1175/JHM-D-14-0177.1, 2015.

857 Margulis, S. A., Fang, Y., Li, D., Lettenmaier, D. P., and Andreadis, K.: The Utility of
858 Infrequent Snow Depth Images for Deriving Continuous Space-Time Estimates of Seasonal
859 Snow Water Equivalent, Geophysical Research Letters, 46, 5331–5340,
860 https://doi.org/10.1029/2019GL082507, 2019.

861 Marti, R., Gascoin, S., Berthier, E., De Pinel, M., Houet, T., and Laffly, D.: Mapping snow
862 depth in open alpine terrain from stereo satellite imagery, The Cryosphere, 10, 1361–1380,
863 https://doi.org/10.5194/tc-10-1361-2016, 2016.

864 Matheson, J. E. and Winkler, R. L.: Scoring Rules for Continuous Probability Distributions,
865 Management Science, 22, 1087–1096, https://doi.org/10.1287/mnsc.22.10.1087, 1976.

866 Mazzolini, M., Aalstad, K., Alonso-González, E., Westermann, S., and Treichler, D.: Spatio-
867 temporal snow data assimilation with the ICESat-2 laser altimeter,
868 https://doi.org/10.5194/egusphere-2024-1404, 24 May 2024.

869 McGrath, D., Webb, R., Shean, D., Bonnell, R., Marshall, H., Painter, T. H., Molotch, N. P.,
870 Elder, K., Hiemstra, C., and Brucker, L.: Spatially Extensive Ground-Penetrating Radar Snow
871 Depth Observations During NASA's 2017 SnowEx Campaign: Comparison With In Situ,
872 Airborne, and Satellite Observations, Water Resources Research, 55, 10026–10036,
873 https://doi.org/10.1029/2019WR024907, 2019.

874 Molotch, N. P. and Bales, R. C.: SNOTEL representativeness in the Rio Grande headwaters
875 on the basis of physiographics and remotely sensed snow cover persistence, Hydrological
876 Processes, 20, 723–739, https://doi.org/10.1002/hyp.6128, 2006.

877 Nagler, T., Rott, H., Ripper, E., Bippus, G., and Hetzenecker, M.: Advancements for
878 Snowmelt Monitoring by Means of Sentinel-1 SAR, Remote Sensing, 8, 348,
879 https://doi.org/10.3390/rs8040348, 2016.

880   Oveisgharan, S., Zinke, R., Hoppinen, Z., and Marshall, H. P.: Snow water equivalent
881   retrieval over Idaho – Part 1: Using Sentinel-1 repeat-pass interferometry, The Cryosphere,
882   2024.

883   Painter, T. H., Berisford, D. F., Boardman, J. W., Bormann, K. J., Deems, J. S., Gehrke, F.,
884   Hedrick, A., Joyce, M., Laidlaw, R., Marks, D., Mattmann, C., McGurk, B., Ramirez, P.,
885   Richardson, M., Skiles, S. M., Seidel, F. C., and Winstral, A.: The Airborne Snow
886   Observatory: Fusion of scanning lidar, imaging spectrometer, and physically-based
887   modeling for mapping snow water equivalent and snow albedo, Remote Sensing of
888   Environment, 184, 139–152, https://doi.org/10.1016/j.rse.2016.06.018, 2016.

889   Raleigh, M. S. and Small, E. E.: Snowpack density modeling is the primary source of
890   uncertainty when mapping basin-wide SWE with lidar, Geophysical Research Letters, 44,
891   3700–3709, https://doi.org/10.1002/2016GL071999, 2017.

892   Rittger, K., Bair, E. H., Kahl, A., and Dozier, J.: Spatial estimates of snow water equivalent
893   from reconstruction, Advances in Water Resources, 94, 345–363,
894   https://doi.org/10.1016/j.advwatres.2016.05.015, 2016.

895   Slater, A. G., Barrett, A. P., Clark, M. P., Lundquist, J. D., and Raleigh, M. S.: Uncertainty in
896   seasonal snow reconstruction: Relative impacts of model forcing and image availability,
897   Advances in Water Resources, 55, 165–177,
898   https://doi.org/10.1016/j.advwatres.2012.07.006, 2013.

899   Smyth, E. J., Raleigh, M. S., and Small, E. E.: Particle Filter Data Assimilation of Monthly
900   Snow Depth Observations Improves Estimation of Snow Density and SWE, Water
901   Resources Research, 55, 1296–1311, https://doi.org/10.1029/2018WR023400, 2019.

902   Smyth, E. J., Raleigh, M. S., and Small, E. E.: Improving SWE Estimation With Data
903   Assimilation: The Influence of Snow Depth Observation Timing and Uncertainty, Water
904   Resources Research, 56, https://doi.org/10.1029/2019WR026853, 2020.

905   Smyth, E. J., Raleigh, M. S., and Small, E. E.: The Challenges of Simulating SWE Beneath
906   Forest Canopies are Reduced by Data Assimilation of Snow Depth, Water Resources
907   Research, 58, e2021WR030563, https://doi.org/10.1029/2021WR030563, 2022.

908   Sourp, L., Gascoin, S., Jarlan, L., Pedinotti, V., Bormann, K. J., and Baba, M. W.: Evaluation
909   of high-resolution snowpack simulations from global datasets and comparison with
910   Sentinel-1 snow depth retrievals in the Sierra Nevada, USA, Hydrol. Earth Syst. Sci., 29,
911   597–611, https://doi.org/10.5194/hess-29-597-2025, 2025.

912   Sturm, M. and Liston, G. E.: Revisiting the Global Seasonal Snow Classification: An
913   Updated Dataset for Earth System Applications, Journal of Hydrometeorology,
914   https://doi.org/10.1175/JHM-D-21-0070.1, 2021.

915   Treichler, D. and Kääb, A.: Snow depth from ICESat laser altimetry — A test study in
916   southern Norway, Remote Sensing of Environment, 191, 389–401,
917   https://doi.org/10.1016/j.rse.2017.01.022, 2017.

918   Trujillo, E. and Molotch, N. P.: Snowpack regimes of the Western United States, Water
919   Resources Research, 50, 5611–5623, https://doi.org/10.1002/2013WR014753, 2014.

920   USDA,NRCS: SNO$_{TEL}$ Data, 2024.

921